Instability of Dirac semimetal phase under a strong magnetic field

Zhida Song,[1,2] Zhong Fang,[1,3] and Xi Dai[1,3,*]

[1]*Beijing National Laboratory for Condensed Matter Physics and Institute of Physics, Chinese Academy of Sciences, Beijing 100190, China*
[2]*University of Chinese Academy of Sciences, Beijing 100049, China*
[3]*Collaborative Innovation Center of Quantum Matter, Beijing 100084, China*

The quantum limit can be easily reached in Dirac semimetals under a magnetic field, which leads to some exotic many-body physics due to the high degeneracy of the topological zeroth Landau bands. By solving the effective Hamiltonian, which is derived by tracing out the high-energy degrees of freedom, at the self-consistent mean-field level, we have systematically studied the instability of Dirac semimetals under a strong magnetic field. A charge-density wave (CDW) phase and a polarized nematic phase formed by "exciton condensation" are predicted as the ground state for the tilted and untilted bands, respectively. Furthermore, we propose that, as distinguished from the CDW phase, the nematic phase can be identified in experiments by anisotropic transport and Raman scattering.

I. INTRODUCTION

Searching for new states of matter in solid materials is one of the key problems in condensed-matter physics and has attracted lots of research interest recently. Applying an external magnetic field has provided an additional dimension for such studies, already leading to surprisingly rich phenomena and phases in two-dimensional electron-gas systems, e.g., the integer [1] and fractional [2] quantum Hall effects, the Wigner crystal phase, as well as the nematic phases [3–5]. The high degeneracy of Landau levels resulting from the Landau quantization of the electronic wave functions is the main origin of the instability towards the various exotic phases mentioned above. In three-dimensional systems, the Landau quantization only happens in the plane perpendicular to the magnetic field and the energy dispersion along the field direction remains unchanged. For ordinary semiconductor systems with quadratic band dispersion, the high degeneracy of the Landau bands (LBs) leads to almost perfect nesting of the "Fermi surfaces" along the field direction, as illustrated schematically in Fig. 1. Such a nesting effect will be greatly enhanced in the so-called quantum limit, where only the lowest LB cuts through the Fermi level, and the field-induced symmetry-breaking phases such as charge-density waves (CDWs) [6–8], spin-density waves [6,9,10], and valley-density waves [10], will be stabilized as the ground state.

It is very difficult to reach the quantum limit in normal semiconductors and semimetals and the experimental observation of the field-induced CDW phase in real materials, i.e., Bi and Sb, is still under debate [11,12]. The recently discovered topological semimetals provide a new platform for the search for new exotic phenomena under magnetic fields [13–21]. For Dirac [22–24] or Weyl [25–31] semimetals, where the Fermi level is very close to the Dirac or Weyl points, the quantum limit can be easily reached even under a weak magnetic field and more fruitful many-body physics can be realized due to the extra valley and orbital degrees of freedom [32,33]. For instance, in a strong magnetic field, the Weyl semimetal is

found to be stabilized as a chiral-symmetry-breaking CDW state [34,35]. In the present paper, we systematically study the possible instabilities of Dirac semimetal state under a magnetic field in the quantum limit. We find that, besides the CDW phase, a new state, the polarized nematic phase, can be stabilized in a large part of the phase diagram. Such an exotic phase is caused by the "exciton condensation" between the two zeroth LBs, which breaks both the rotational symmetry and the inversion symmetry, leading to a number of important physical consequences in transport and optical experiments.

II. MODEL

Dirac semimetals can be divided into two categories by whether the Dirac points (DPs) are located on high-symmetry lines or points [24] of the Brillouin zone (BZ). In this paper, we focus on the first category, where the DPs are protected by the crystalline symmetry along the high-symmetry lines and always appear in pairs due to the presence of time-reversal symmetry. The typical example of such types of materials is Na_3Bi [23], where the DPs are generated by the crossings of two doubly degenerate bands along the z axis. The low-energy physics of such a type of Dirac semimetal can be well described by the following k · p model:

$$H^0 = C(k_z) + \begin{pmatrix} M(k_z) & -v\hbar k_- & \gamma(\mathbf{k}) & 0 \\ -v\hbar k_+ & -M(k_z) & 0 & \gamma(\mathbf{k}) \\ \gamma^*(\mathbf{k}) & 0 & -M(k_z) & v\hbar k_- \\ 0 & \gamma^*(\mathbf{k}) & v\hbar k_+ & M(k_z) \end{pmatrix}.$$

(1)

Here $C(k_z) = C_0(\cos a_0 k_z - \cos a_0 k_c)$, $M(k_z) = M_0(\cos a_0 k_z - \cos a_0 k_c)$, $k_\pm = k_x \pm i k_y$, v is the velocity in xy plane, a_0 is the lattice along k_z, and $\pm k_c$ are the locations of DPs. The bases of the k · p model can be labeled by their main orbital characters as $|P\frac{3}{2}\rangle$, $|S\frac{1}{2}\rangle$, $|S-\frac{1}{2}\rangle$, $|P-\frac{3}{2}\rangle$, respectively. The first term in Eq. (1) plays an important role in the formation of type-II Weyl points [36,37]. As long as $|C_0| < |M_0|$, which is the case we focus on, the $C(k_z)$ term will just tilt the DPs and change the ellipsoidal Fermi surface to a pyriform one. Even so, as shown in the following, this term will play an important role in determining whether the
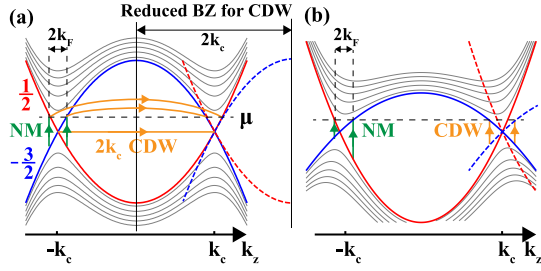
---

*daix@aphy.iphy.ac.cn

FIG. 1. Band structure and instability channels. The two zeroth LBs, referred to as the conductance and valence bands, are plotted in red and blue, respectively, and the high-energy LBs are plotted in gray. Panel (a) shows the nematic phase channel (green arrows) and three CDW phase channels (orange arrows) in an untilted band structure ($C_0 = 0$). As argued in the text, only the nematic phase and the $2k_c$ CDW phase can be realized in the low-density limit. Here the dashed colored lines represent the folded bands in the $2k_c$ CDW phase. Panel (b) shows the two channels in a tilted band structure ($C_0 \neq 0$). It is apparent that the kinetic-energy cost of the $2k_c$ CDW order is significantly lowered by the tilting.

CDW or nematic phase will be stabilized. The high-order term $\gamma(\mathbf{k})$ does not play any important role for the physics discussed here and so is neglected in the rest of the paper.

The external magnetic field B is applied along the z direction. We adopt the Landau gauge $\mathbf{A} = (-yB, 0, 0)$, which leaves k_x and k_z still as good quantum numbers, so the LB eigenenergies and eigenstates can be solved analytically (see Appendix A). As shown in Fig. 1, the two zeroth LBs disperse linearly and cross with each other at the DPs. The quantum limit can be reached by increasing the magnetic field such that only the zeroth LBs cuts through the Fermi level. In the present work we are only interested in the instability in the quantum limit, so we only keep the zeroth LBs in the noninteracting Hamiltonian,

$$\hat{H}^0 = \sum_{ak_xk_z} \epsilon_{k_za} \hat{\psi}^\dagger_{k_xk_za} \hat{\psi}_{k_xk_za}, \tag{2}$$

$$\epsilon_{k_za} = \begin{cases} C(k_z) - M(k_z), & a = c \\ C(k_z) + M(k_z), & a = v. \end{cases} \tag{3}$$

Here c and v represent the conduction band [red band in Fig. 1] and valence band [blue band in Fig. 1], which is formed by the $|S\frac{1}{2}\rangle$ and $|P - \frac{3}{2}\rangle$ states, respectively. Since they belong to different eigenvalues of C_6, the crossings at $\pm k_c$ are protected by rotational symmetry and will persist even if nonzero $\gamma(\mathbf{k})$ is present.

Notice that the Zeeman's coupling between the magnetic field and the field-free orbitals is neglected here. In a first-principle study of the effective g factor [38], we show that the Zeeman splitting in a typical Dirac semimetal under a magnetic field as strong as 100 T is just about 5 meV, which is much smaller than the band inversion energy M_0 and so would not affect the discussion qualitatively.

III. EFFECTIVE INTERACTION

To explore the stability of the above system under the Coulomb repulsive interaction, we need to derive an effective

interaction for the zeroth LBs by tracing out all the high LBs. Taking the random-phase approximation (RPA), we get

$$\hat{H}^{\text{eff}}_{\text{int}} = \frac{1}{2\Omega} \sum_{\mathbf{q} \neq 0} \sum_{k_x k_z} \sum_{p_x p_z} \sum_{ab} e^{il_B^2 q_y(k_x - p_x)} W(\mathbf{q})$$

$$\times \hat{\psi}^\dagger_{k_x+q_x, k_z+q_z, a} \hat{\psi}^\dagger_{p_x, p_z, b} \hat{\psi}_{p_x+q_x, p_z+q_z, b} \hat{\psi}_{k_x, k_z, a}, \tag{4}$$

$$W(\mathbf{q}) = \frac{e^2}{\epsilon_0 \kappa(\mathbf{q})\mathbf{q}^2} e^{-\frac{1}{2}l_B^2 \mathbf{q}_\perp^2}, \tag{5}$$

where $\mathbf{q}_\perp = (q_x, q_y)$, $l_B = \sqrt{\hbar/eB}$ is the magnetic length, $\kappa(\mathbf{q})$ is the effective dielectric function, and Ω is the sample volume. Details of the RPA derivation and the discussion of the dielectric function are given in Appendix B. As shown below, the long-wave part of the interaction contributes the most in both of the possible instabilities, thus we can approximate $\kappa(\mathbf{q})$ by a dielectric constant $\kappa = \kappa_0 + \frac{1}{3}\kappa_z + \frac{2}{3}\kappa_{xy}$, where

$$\kappa_z \approx \frac{e^2 u}{3\pi^2 \epsilon_0 v^2 \hbar} \left[0.9 + \ln\left(\frac{M_0 l_B}{v\hbar} \right) \right], \tag{6}$$

$$\kappa_{xy} \approx \frac{e^2}{4\pi^2 \epsilon_0 u \hbar} \left[0.6 + \ln\left(\frac{M_0 l_B}{v\hbar} \right) \right] \tag{7}$$

are the dielectric constants from high LBs, κ_0 is the dielectric constant from the core electrons, and $u = \frac{1}{\hbar} M_0 a_0 \sin(a_0 k_c)$ is the Dirac velocity along the z direction. The derivation of such dielectric constants is given in Appendix C. It should be noted that the results in Eq. (6) and (7) are not only applied to this particular model, in fact they are universal for all the Dirac or Weyl semimetals. One of the important features for the above effective interaction is that its strength can be tuned by an external magnetic field, which is a bit unusual in condensed-matter physics. The mechanism is easy to understand; that is, the energy gap between the zeroth and high LBs increases with the field strength, which weakens the screening effect.

IV. COULOMB HOLE PLUS SCREENED EXCHANGE METHOD

It is well known that the direct Hartree–Fock mean-field approximation for metals with a long-range Coulomb interaction leads to a singular Fermi velocity because of a logarithmic divergence in the exchange channel. To handle this problem, we adopt the "Coulomb hole plus screened exchange" (COHSEX) method, which is a simplified version of the GW method [39]. Applying this method to our model, the self-energy consists of a direct Hartree term Σ^{H} and a screened exchange term Σ^{E} where the interaction is not only screened by high-LB electrons but also the zeroth-LB electrons. As explained in the next section, in the limit of low carrier density, the system has a CDW instability at $Q = 2k_c$. For convenience of calculation, we take the commensurate limit by setting $k_c = \frac{\pi}{D_c a_0}$, where D_c is an integer. The BZ will be folded D_c times if the CDW order is present. Thus, in general, we can define the Green's function as $G_{an,bm}(k_x, \bar{k}_z, t) = \langle T_t \hat{\psi}_{k_x, \bar{k}_z+nQ, a}(t) \hat{\psi}^\dagger_{k_x, \bar{k}_z+mQ, b}(0) \rangle$, where $n, m = 0, \ldots, D_c - 1$ is the sub-BZ index and $\bar{k}_z$ takes values in the reduced BZ: $0 \leqslant \bar{k}_z < Q$.
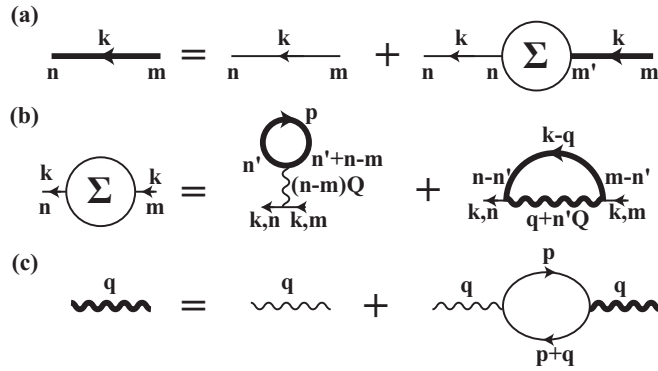
FIG. 2. Feynman diagrams for the COHSEX method. The full and free Green's functions are represented by thick and thin lines, respectively. Correspondingly, the screened effective interaction W^S and the bare effective interaction W are represented by thick and thin wavy lines, respectively. Panel (a) shows the diagram for Dyson's equation. Panel (b) shows the diagram for the self-energy. Panel (c) shows the diagram for the screened effective interaction, where the Green's functions participating in the screening are approximated by the free Green's functions.

Then the self-energy can be expressed as [Fig. 2(b)]

$$\Sigma^{\text{H}}_{an,bm}(k_x k_z) = \delta_{ab} W(0,0,(n-m)Q) \int \frac{dp_x dp_z d\omega}{(2\pi)^3}$$
$$\times \sum_{cn'} G_{c,n'+n-m;c,n'}(p_x, p_z, \omega) e^{i\omega 0^+}, \quad (8)$$

$$\Sigma^{\text{E}}_{an,bm}(k_x k_z) = -\sum_{n'} \int \frac{d^2\mathbf{q}_\perp}{(2\pi)^2} \int \frac{dp_z d\omega}{(2\pi)^2}$$
$$\times W^{\text{S}}(\omega = 0, \mathbf{q}_\perp, k_z - p_z + n'Q)$$
$$\times G_{a,n-n';b,m-n'}(k_x - q_x, p_z, \omega) e^{i\omega 0^+}, \quad (9)$$

where $W^{\text{S}}(\omega = 0)$ is the *static* screened interaction. Here we approximate the Green's-function screening W^{S} by the free Green's function at zero doping, as shown in Fig. 2(c). Such an approximated screened interaction can be derived analytically

$$W^{\text{S}}(\omega = 0, \mathbf{q}) = \frac{e^2}{\epsilon_0} \frac{e^{-\frac{1}{2} l_B^2 \mathbf{q}_\perp^2}}{\kappa \mathbf{q}^2 + q_{\text{TF}}^2(q_z) e^{-\frac{1}{2} l_B^2 \mathbf{q}_\perp^2}}, \quad (10)$$

where $q_{\text{TF}}(q_z)$ is the effective Thomas–Fermi wave vector,

$$q_{\text{TF}}^2(q_z) = \frac{e^2 M_0 \ln \left| \frac{\sin ak_c + \sin \frac{aq_z}{2}}{\sin ak_c - \sin \frac{aq_z}{2}} \right|}{2\epsilon_0 \pi^2 l_B^2 (M_0^2 - C_0^2) a \sin \frac{aq_z}{2}}. \quad (11)$$

We have checked this approximation by comparing it with full self-consistent calculations, where W^{S} is calculated from G self-consistently, and find that the correction of the results is very small.

With the above approximation, Dyson's equation $(\hat{G}^{0-1} - \hat{\Sigma})\hat{G} = \mathbb{I}$ [Fig. 2(a)] and Eqs. (8) and (9) set up a self-consistent loop to determine the possible symmetry-breaking phases at zero temperature by assuming different nondiagonal matrix elements in the self-energy matrix. For convenience, we define the order parameter as $\Delta_{an,bm}(k_x, k_z) = \langle \psi^\dagger_{an}(k_x, k_z) \psi_{bm}(k_x, k_z) \rangle$, whose nondiagonal
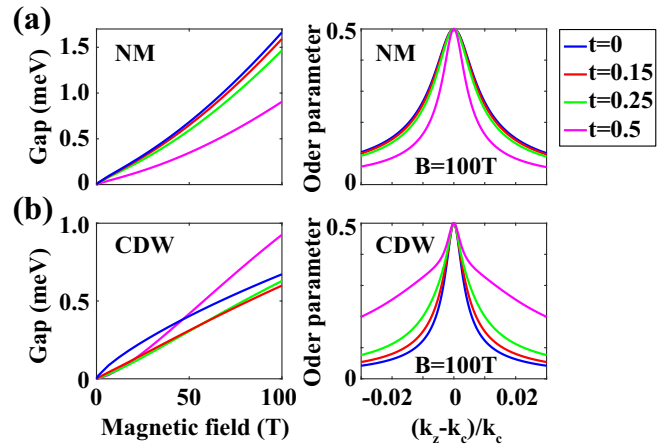

FIG. 3. In the left panel, the energy gaps of the polarized nematic and CDW phases at zero doping and a few tilting ratios are plotted as functions of magnetic field. In the right panel, the corresponding order parameters of the two phases at $B = 100$ T, i.e., $|\Delta^{\text{NM}}_{v;c}(k_z)|$ and $(\sum_a |\Delta^{\text{CDW}}_{a,-1;a,0}|^2)^{1/2}$, are plotted around the DPs.

elements in the band indexes a, b and sub-BZ indexes n, m denote the appearance of the nematic phase and the CDW phase, respectively.

V. CHARGE-DENSITY-WAVE PHASE

The CDW phase acquires its instability from the Fermi-surface nesting in the quasi-one-dimensional band structure [Fig. 1]. At first sight, it seems that the CDW should occur simultaneously at the $Q = 2k_c + 2k_F$ and $Q = 2k_c - 2k_F$ channels for conduction and valence bands, respectively. However, the interband Hartree energy can lock the CDWs in different bands to the same $Q = 2k_c$, at least for low enough carrier density. This conclusion can be reached by simply comparing the energy difference between the CDW phases with $Q = 2k_c \pm 2k_F$ and $Q = 2k_c$. According to Eq. (8), the $Q = 2k_c$ phase gains an extra interband Hartree energy of $\sim W(Q)\text{Re}(\Delta^{\text{CDW}}_{c0,c-1}\Delta^{\text{CDW}*}_{v0,v-1})$, which reaches a negative constant as k_F approaches zero if $\Delta^{\text{CDW}}_{c0,c-1} = -\Delta^{\text{CDW}}_{v0,v-1}$. The kinetic energy and exchange energy [Eq. (9)] difference between the $Q = 2k_c$ and the $Q = 2k_c \pm 2k_F$ phases vanish as k_F approaches zero. Therefore, as long as k_F is small enough, the CDW phase with $Q = 2k_c$ for both bands will be stabilized.

The numerical calculation is performed with the initial condition $\Delta^{\text{CDW}}_{an,bm}(k_x, k_z) = \delta_{n,m+1}\eta_{a,b}(k_z) + \delta_{n+1,m}\eta^*_{b,a}(k_z)$, where $\eta(k_z)$ is a random matrix. The parameters are set as $\kappa_0 = 5$, $a_0 = 9.66$ Å, $M_0 a_0 = 2.3$ eV Å, $\hbar v = 2.0$ eV Å, and $D_c = 4$, which give the same Dirac velocity for Na$_3$Bi as the first-principle results [23]. We set C_0 as $C_0 = -t M_0$, where $t \in [0,1)$ is the tilting ratio describing how much the bands are tilted. In Fig. 3(b), we plot the band gaps and order parameters at various tilting ratios and magnetic fields. It shows that the tilting can significantly enlarge the CDW order, which is a direct consequence of saving the kinetic energy, as sketched in Fig. 1(b). The typical band gap under a strong magnetic field is about 1 meV and so correspond to a transition temperature of about 10 K.
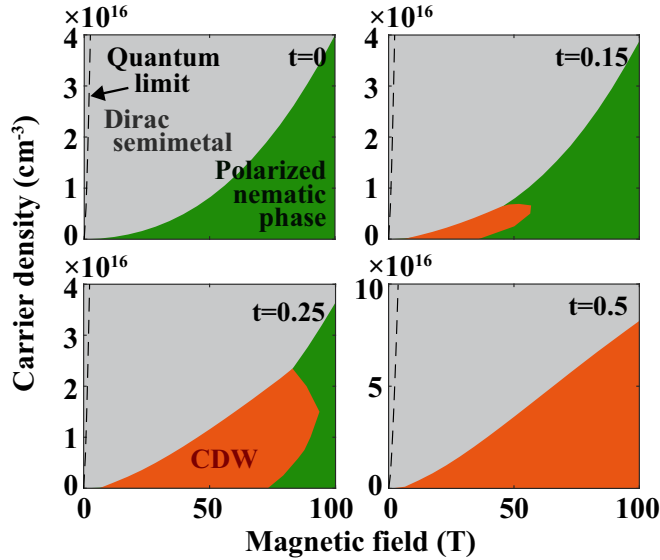
FIG. 4. The phase diagram in density-field parameter space at a few tilting ratios. Here the critical field to achieve the quantum limit is indicated by dashed lines, and the Dirac semimetal, polarized nematic, and CDW phases are represented by gray, green, and orange areas, respectively. It shows that the polarized nematic phase is more favored in untilted bands, while the CDW phase is more favored in tilted bands.

VI. NEMATIC PHASE

As shown in Fig. 1, if the chemical potential is close enough to the DPs, a rotation-broken phase, i.e., the nematic phase, can be stabilized. Since the nematic phase does not break the translational symmetry, its order parameter can be expressed in the full BZ as $\Delta_{a,b}^{\mathrm{NM}}(k_x,k_z) = \delta_{\bar{a}b}\eta(k_z)$, where $-\pi \leqslant k_z < \pi$, and $\bar{a} = v(c)$ for $a = c(v)$. Two different types of η can be obtained: odd or even with respect to k_z. According to the definition of the LB wave function [Eq. (A2)], the inversion operator acts on it as

$$\mathcal{P}\hat{\psi}_{k_x,k_z,c}^{\dagger}\hat{\psi}_{k_x,k_z,v}\mathcal{P}^{-1} = -\hat{\psi}_{-k_x,-k_z,c}^{\dagger}\hat{\psi}_{-k_x,-k_z,v}, \quad (12)$$

thus the even and odd η will respectively break and maintain the inversion symmetry. As discussed in the next paragraph, the inversion-broken phase, which will be referred to as the polarized nematic phase in the following, is always more favored.

The band gaps and order parameters of the polarized nematic phase, and the phase diagram consisting of the phases mentioned above, are calculated with the same parameters used for the CDW phase and shown in Fig. 3(a) and 4, respectively, which indicates that the polarized nematic phase is more favored in untilted bands while the CDW phase is more favored in tilted bands. This can be understood as a result of competition between kinetic energy and interaction energy. On one hand, as explained latter, the polarized nematic phase has a lower interaction energy; on the other hand, as shown in Fig. 1(b), the tilting will significantly lower the kinetic-energy cost in the CDW phase. Therefore, as shown in Fig. 4, the area of the polarized nematic phase in the phase diagram will shrink and eventually vanish with

increasing tilting. Now let us explain why the polarized nematic phase has a lower interaction energy. Since its Hartree energy reaches zero, i.e., the minimum, we only need to compare the exchange energies. Equation (9) suggests that the exchange energy in the CDW phase is approximately $-W^{\mathrm{S}}(\mathbf{q}_{\perp},0)|\Delta_{a,0;a,-1}^{\mathrm{CDW}}|^2$. While the exchange energy in the nematic phase consists of three parts: two intravalley parts $-\frac{1}{2}W^{\mathrm{S}}(\mathbf{q}_{\perp},0)|\Delta_{a\bar{a}}^{\mathrm{NM}}(\pm k_c)|^2$, which equal the CDW part; and an intervalley part $-W^{\mathrm{S}}(\mathbf{q}_{\perp},Q)\mathrm{Re}(\Delta_{a\bar{a}}^{\mathrm{NM}}(k_c)\Delta_{a\bar{a}}^{\mathrm{NM}*}(-k_c))$, which is negative in the polarized nematic phase [$\Delta_{a\bar{a}}^{\mathrm{NM}}(k_c) = \Delta_{a\bar{a}}^{\mathrm{NM}}(-k_c)$]. Here we have omitted the summation and integral symbols for brevity. Thus we conclude that the polarized nematic order has a lower interaction energy than the inversion symmetric nematic order and the CDW order.

Another aspect to understand this nematic order is to view it as a "pairing order" between electrons in the conduction band and holes in the valence band, which is the "exciton condensation" state in the mean-field level [40]. Formally, we can rewrite the creation operators of electrons and holes as $\psi_{k_x,k_z,c}^{\dagger} = \psi_{k_x,k_z}^{\mathrm{e}\dagger}$, $\psi_{k_x,k_z,v} = \psi_{-k_x,-k_z}^{\mathrm{h}\dagger}$ and rewrite the order parameter as a pairing order $\langle\psi_{k_x,k_z}^{\mathrm{e}\dagger}\psi_{-k_x,-k_z}^{\mathrm{h}\dagger}\rangle$. Then the exchange interaction turns into an effective attractive interaction between electrons in the conduction band and holes in the valence band. And our mean-field theory is equivalent to the BCS theory for superconductivity. Since the system is three dimensional, the quantum fluctuation and disorder cannot suppress the phase coherence completely and such a transition can survive even beyond the mean-field approximation.

VII. EXPERIMENTAL ASPECTS

The most direct consequence of both the nematic and CDW phase transitions is the opening of an energy gap between the zeroth LBs, which can be observed easily through the transport measurement. For the CDW phase, since the order wave vector given by the distance between two DPs is in general incommensurate with the lattice, the corresponding Goldstone mode, i.e., the so-called sliding mode, will contribute to an electric-field-dependent conductivity along the wave-vector direction due to the depinning effect [41]. For the nematic phase, an anisotropic resistance in the xy plane is expected due to the rotational symmetry breaking. Since the original rotational symmetry is discrete, the corresponding Goldstone mode in the nematic phase will be gapped and can be detected by neutron-scattering experiments.

Another piece of evidence for the nematic phase should be the anisotropy in the inelastic light scattering shown in Fig. 5(a), where a strongly anisotropic scattering section with a Raman shift of the band gap will be observed, since both the initial and final states are rotation broken.

To verify this, we apply a numerical study of the Raman-scattering section with the formula $\frac{\partial^2\sigma}{\partial\Omega\partial\omega_s} \propto \sum_F |M_{F,G}|^2\delta(E_F - E_I - \hbar\Omega)$ where $\Omega = \omega_i - \omega_s$ is the Raman shift and $M_{F,I}$ is the light scattering matrix element [42]:

$$M_{F,I} = \mathbf{e}_i \cdot \mathbf{e}_s \langle F|\hat{\rho}|G\rangle + \frac{1}{m}\sum_J \left[\frac{\langle F|\hat{\pi}^s|J\rangle\langle J|\hat{\pi}^i|G\rangle}{E_G - E_J + \omega_i} \right.$$

$$\left. + \frac{\langle F|\hat{\pi}^i|J\rangle\langle J|\hat{\pi}^s|G\rangle}{E_G - E_J - \omega_s} \right]. \quad (13)$$
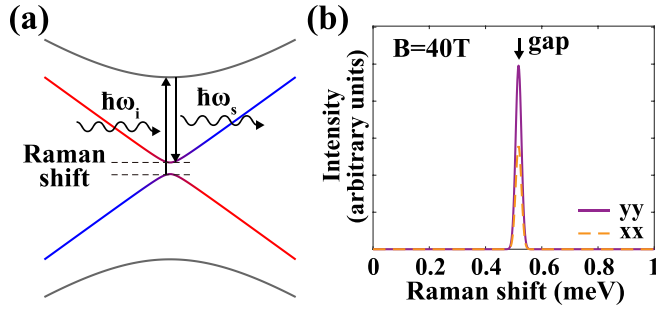
FIG. 5. Raman scattering characterizing the nematic phase. In panel (a) the scattering process that reveals the rotation symmetry breaking is sketched. In panel (b) the numerical differential scattering section at zero doping and $B = 40$ T is shown.

Here $|G\rangle$, $|J\rangle$, and $|F\rangle$ represent the initial (ground), intermediate, and final many-body states having energies E_G, E_J, and E_F, respectively. i, s represent the polarization direction of the initial and scattered photons, respectively. And $\hat{\rho}$, $\hat{\pi}$ are the density and velocity operators in second-quantization form, respectively. Results at zero doping and field $B = 40$ T are shown in Fig. 5(b), where the large splitting in the xx and yy polarized light measurements indicates the rotation-symmetry breaking.

VIII. SUMMARY

In summary, we have systematically studied the instabilities of the Dirac semimetal phase in the quantum limit due to the Coulomb interaction. The high-LB electrons far away from the Fermi level are considered as a background to screen the interaction by an effective dielectric constant in the long-wavelength limit. All possible instabilities on the zeroth LBs, i.e., the inter- and intravalley and inter- and intraband channels, are treated within the so-called COHSEX method. By numerical calculations, we have shown that a polarized nematic phase breaking both the rotational and inversion symmetry and a CDW phase breaking translational symmetry will be stabilized depending on the strength of the tilting terms for the Dirac cones. Relevant experiments, including transport and Raman scattering, are also proposed to verify the existence of such phases. Further theoretical studies on the physical properties such as magnetotransport in these exotic phases are also strongly encouraged.

APPENDIX A: SOLUTION OF THE FREE HAMILTONIAN

The eigenenergies and eigenstates of our model Hamiltonian can be explicitly derived as [43]

$$
\epsilon_{k_z s\alpha} = \begin{cases} C(k_z) + \sqrt{M^2(k_z) + 2\hbar^2 v^2 l_B^{-2}|\alpha|}, & \alpha > 0 \\ C(k_z) - s M(k_z), & \alpha = 0 \\ C(k_z) - \sqrt{M^2(k_z) + 2\hbar^2 v^2 l_B^{-2}|\alpha|}, & \alpha < 0, \end{cases} \quad \text{(A1)}
$$

$$
\hat{\psi}^\dagger_{k_x k_z s\alpha} = \frac{1}{\sqrt{l_z l_x}} \sum_{j_z} \delta_{s,\text{sign}(j_z)} C^{k_z s\alpha}_{j_z}
$$
$$
\times \int d^3\mathbf{r}\, e^{i(k_z z + k_x x)} H_{\alpha'}\left(\frac{y}{l_B} - l_B k_x\right) \hat{\psi}^\dagger_{j_z}(\mathbf{r}), \quad \text{(A2)}
$$

where $s = 1(-1)$ represents the upper left (lower right) block in the Hamiltonian, $\alpha = 0, \pm 1, \dots$ is the LB index, $j_z = \frac{3}{2}, \frac{1}{2}, -\frac{1}{2}, -\frac{3}{2}$ is the k · p-basis index, and $H_{\alpha'}$ is the α'th-order one-dimensional harmonic oscillator. Here α' is defined as $\alpha' = |\alpha| + s - j_z - \frac{1}{2}$, which equals $|\alpha| - 1$, $|\alpha|$, $|\alpha| - 1$, $|\alpha|$ for $j_z = \frac{3}{2}, \frac{1}{2}, -\frac{1}{2}, -\frac{3}{2}$, respectively, and $\alpha' = -1$ terms should be omitted. The coefficient $C^{k_z s\alpha}_{j_z}$ is defined as

$$
C^{k_z,+1,\alpha}_{\frac{3}{2}} = \cos\frac{\theta}{2}, \quad C^{k_z,+1,\alpha}_{\frac{1}{2}} = \sin\frac{\theta}{2},
$$
$$
C^{k_z,-1,\alpha}_{-\frac{1}{2}} = -\sin\frac{\theta}{2}, \quad C^{k_z,-1,\alpha}_{-\frac{3}{2}} = \cos\frac{\theta}{2}, \quad \text{(A3)}
$$

for $\alpha > 0$,

$$
C^{k_z,+1,\alpha}_{\frac{3}{2}} = -\sin\frac{\theta}{2}, \quad C^{k_z,+1,\alpha}_{\frac{1}{2}} = \cos\frac{\theta}{2},
$$
$$
C^{k_z,-1,\alpha}_{-\frac{1}{2}} = \cos\frac{\theta}{2}, \quad C^{k_z,-1,\alpha}_{-\frac{3}{2}} = \sin\frac{\theta}{2}, \quad \text{(A4)}
$$

for $\alpha < 0$, and

$$
C^{k_z,+1,\alpha}_{\frac{3}{2}} = 0, \quad C^{k_z,+1,\alpha}_{\frac{1}{2}} = 1,
$$
$$
C^{k_z,-1,\alpha}_{-\frac{1}{2}} = 0, \quad C^{k_z,-1,\alpha}_{-\frac{3}{2}} = 1, \quad \text{(A5)}
$$

for $\alpha = 0$, respectively, where the auxiliary angle θ is set by

$$
\theta = \arctan\frac{v\hbar\sqrt{2|\alpha|}}{M(k_z)l_B}, \quad 0 \leqslant \theta < \pi.
$$

The conduction and valence bands in the paper are the $\alpha = 0$, $s = 1$ and $\alpha = 0$, $s = -1$ bands here.

APPENDIX B: EFFECTIVE INTERACTION ON THE ZEROTH LANDAU BANDS

In this section, we derive the effective interaction on the zeroth LBs by tracing out the high LBs in RPA. The long-range Coulomb interaction can be written as

$$
\hat{H}_{\text{int}} = \frac{1}{2} \sum_{j_z j'_z} \int d^3\mathbf{r} \int d^3\mathbf{r}' \frac{e^2}{4\pi \epsilon_0 \kappa_0 |\mathbf{r} - \mathbf{r}'|}
$$
$$
\times \hat{\psi}^\dagger_{j_z}(\mathbf{r}) \hat{\psi}^\dagger_{j'_z}(\mathbf{r}') \hat{\psi}_{j'_z}(\mathbf{r}') \hat{\psi}_{j_z}(\mathbf{r}), \quad \text{(B1)}
$$

where κ_0 is the dielectric constant contributed by the core electron states. By a representation transformation, the interaction can be written on the LB bases,

$$
\hat{H}_{\text{int}} = \frac{1}{2\Omega} \sum_{\mathbf{q}\neq 0} \sum_{k_x k_z} \sum_{p_x p_z} \sum_{ss'} \sum_{\alpha\beta\alpha'\beta'} e^{il_B^2 q_y(k_x - p_x)}
$$
$$
\times U_{k_z s\alpha\alpha', p_z s'\beta\beta'}(\mathbf{q}) \hat{\psi}^\dagger_{k_x+q_x, k_z+q_z, s\alpha'} \hat{\psi}^\dagger_{p_x, p_z, s'\beta}
$$
$$
\times \hat{\psi}_{p_x+q_x, p_z+q_z, s'\beta'} \hat{\psi}_{k_x, k_z, s\alpha}, \quad \text{(B2)}
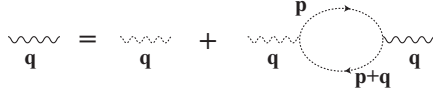$$

FIG. 6. RPA diagrams of the effective interaction on the zeroth LBs. The solid wavy line represents the effective interaction, while the dashed wavy line represents the bare interaction. The dashed straight line represents the Green's functions in high LBs.

where

$$U_{k_z s\alpha\alpha', p_z s'\beta\beta'}(\mathbf{q}) = \frac{e^2}{\epsilon_0 \kappa_0 \mathbf{q}^2} e^{-\frac{1}{2} l_B^2 \mathbf{q}_\perp^2} \Lambda^*_{k_z s\alpha\alpha'}(\mathbf{q}) \Lambda_{p_z s'\beta\beta'}(\mathbf{q}),$$
(B3)

$$\Lambda_{p_z s'\beta\beta'}(\mathbf{q}) = \sum_{j_z} \delta_{s', \text{sign}(j_z)} C^{p_z s'\beta*}_{j_z} C^{p_z+q_z, s'\beta'}_{j_z}$$

$$\times F_{|\beta|+s'-j_z-\frac{1}{2}, |\beta'|+s'-j_z-\frac{1}{2}} \left(\frac{l_B(q_x - iq_y)}{\sqrt{2}} \right).$$
(B4)

Here, $F_{\alpha,\beta}(\xi)$ is the well-known form factor of Landau levels, which is defined as

$$F_{\alpha,\beta}(\xi) = \sqrt{\frac{\beta!}{\alpha!}} \xi^{\alpha-\beta} L_\beta^{(\alpha-\beta)}(|\xi|^2)$$
(B5)

for $\alpha \geqslant \beta$ and $F_{\alpha,\beta}(\xi) = F^*_{\beta,\alpha}(-\xi)$ for $\alpha \leqslant \beta$, and $L_\beta^{(\alpha-\beta)}$ is the Laguerre polynomial [44,45].

In the Feynman diagram representation, the RPA effective interaction on the zeroth LBs can be interpreted as the "dressed" interaction, which has been inserted with bubble diagrams concerning high LBs (Fig. 6). Thus the static effective interactions satisfy

$$W(\mathbf{q}) = U(\mathbf{q}) + U(\mathbf{q}) \chi^{0>}(0 q_x q_z) W(\mathbf{q}),$$
(B6)

where the matrix subscripts are omitted. $\chi^{0>}$ is the bare susceptibility of high LBs:

$$\chi^{0>}_{k_x k_z s\alpha\beta, k'_x k'_z s'\alpha'\beta'}(\omega q_x q_z)$$
$$= \delta_{k_x k'_x} \delta_{k_z k'_z} \delta_{ss'} \delta_{\alpha\alpha'} \delta_{\beta\beta'}$$
$$\times \frac{1}{\Omega} \begin{cases} \frac{n_F(\epsilon_{k_z s\alpha} - \mu) - n_F(\epsilon_{k_z+q_z s\beta} - \mu)}{\omega + \epsilon_{k_z s\alpha} - \epsilon_{k_z+q_z s\beta}} & \alpha, \quad \beta \neq 0 \\ 0 & \text{otherwise.} \end{cases}$$
(B7)

Therefore, the effective interaction can be derived as

$$W_{k_z s, p_z s'}(\mathbf{q}) = \left[U(\mathbf{q}) \left(1 - \frac{\chi^{0>} U(\mathbf{q})}{\Omega} \right)^{-1} \right]_{k_z s 00; p_z s' 00}$$
$$= \frac{e^2}{\epsilon_0 \kappa(\mathbf{q}) \mathbf{q}^2} e^{-\frac{1}{4} l_B^2 \mathbf{q}_\perp^2},$$
(B8)

where

$$\kappa(\mathbf{q}) = \kappa_0 - \frac{e^2}{2\pi \epsilon_0 l_B^2 \mathbf{q}^2} e^{-\frac{1}{2} l_B^2 \mathbf{q}_\perp^2}$$
$$\times \sum_{s\alpha\beta} \int \frac{dk'_z}{2\pi} \Lambda^*_{k'_z s\alpha\beta}(\mathbf{q}) \chi^{0>}_{k'_z s\alpha\beta}(q_z) \Lambda_{k'_z s\alpha\beta}(\mathbf{q})$$
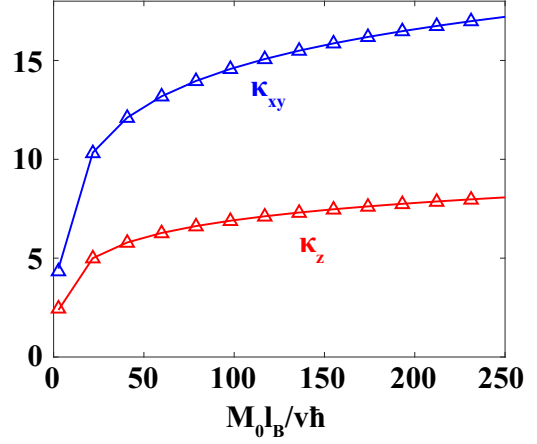(B9)

FIG. 7. The dielectric constants calculated from the definition equations (C3) and (C4) and the simplified equations (C5) and (C6) are plotted by triangles and lines, respectively. It shows that the simplified equations give a very good approximation.

is the effective dielectric function. For brevity, we use here $\chi^{0>}_{k_z s\alpha\beta}(\omega q_z)$ to represent the diagonal elements of $\chi^{0>}$. Because $W_{k_z s, p_z s'}(\mathbf{q})$ does not depend on its subscripts, we denote it as $W(\mathbf{q})$ in this paper.

APPENDIX C: LONG-WAVE BEHAVIOR OF THE EFFECTIVE INTERACTION

In this section, we intend to get a more explicit expression of the dielectric function in the long-wavelength limit. Expanding $\Lambda^*_{k'_z a\alpha\beta}(\mathbf{q}) \chi^{0>}_{k'_z a\alpha\beta}(q_z) \Lambda_{k'_z a\alpha\beta}(\mathbf{q})$ to second order in $\mathbf{q}$, we have

$$\sum_{\alpha\beta} \Lambda^*_{k'_z a\alpha\beta}(\mathbf{q}) \chi^{0>}_{k'_z a\alpha\beta}(q_z) \Lambda_{k'_z a\alpha\beta}(\mathbf{q})$$

$$\approx \sum_\alpha \chi^{0>}_{k'_z a\alpha, -\alpha}(q_z) \left[\frac{1}{4} \left(\frac{\partial \theta_\alpha}{\partial k_z} q_z \right)^2 + \frac{l_B^2 (q_x^2 + q_y^2) \sin^2 \theta_\alpha}{16|\alpha|} \right].$$
(C1)

Substituting in the definition of the auxiliary angle θ_α, we get

$$\kappa(\mathbf{q}) \approx \kappa_0 + \kappa_z \cos^2 \langle \mathbf{q}, \mathbf{B} \rangle + \kappa_{xy} \sin^2 \langle \mathbf{q}, \mathbf{B} \rangle,$$
(C2)

where

$$\kappa_z = \frac{e^2}{8\pi^2 \epsilon_0 l_B^2} \sum_{\alpha=1}^\infty \int \frac{2v^2 \hbar^2 l_B^{-2} \alpha \left(\frac{\partial M(k_z)}{\partial k_z} \right)^2 dk'_z}{\left[M^2(k_z) + 2v^2 \hbar^2 l_B^{-2} \alpha \right]^{\frac{5}{2}}},$$
(C3)

$$\kappa_{xy} = \frac{e^2}{8\pi^2 \epsilon_0 l_B^2} \sum_{\alpha=1}^\infty \int \frac{2v^2 \hbar^2 dk'_z}{4 \left[M^2(k_z) + 2v^2 \hbar^2 l_B^{-2} \alpha \right]^{\frac{3}{2}}},$$
(C4)

and $\langle \mathbf{q}, \mathbf{B} \rangle$ is the angle between $\mathbf{q}$ and the magnetic field. Equations (C3) and (C4) may be simplified further. First, because the main contribution in the k'_z integral comes from small $M(k_z)$, we can expand $M(k_z)$ to linear order of k_z around each DP. Second, the limit $v\hbar l_B^{-1} \ll M_0$ is assumed such that the Landau level splitting is significantly smaller than the bandwidth, so the summation over α can be approximated by integral. Therefore, we achieve the

following formula:

$$\kappa_z \approx \frac{e^2 u}{3\pi^2 \epsilon_0 v^2 \hbar}\left[0.9 + \ln\left(\frac{M_0 l_B}{v\hbar}\right)\right], \qquad (C5)$$

$$\kappa_{xy} \approx \frac{e^2}{4\pi^2 \epsilon_0 u\hbar}\left[0.6 + \ln\left(\frac{M_0 l_B}{v\hbar}\right)\right], \qquad (C6)$$

where $u = \frac{1}{\hbar}M_0 a_0 |\sin(a_0 k_c)|$ is the Dirac velocity along the z direction, and the coefficients 0.9 and 0.6 are obtained by

numerically fitting Eqs. (C5) and (C6) to Eqs. (C3) and (C4). Indeed, Eqs. (C5) and (C6) give very good approximations for Eq. (C3) and (C4) over quite a wide range. In Fig. 7, we compare the two equations with the parameters used in the paper.

In the end, if we neglect the dependence of κ on the direction of **q**, a dielectric constant can be obtained by an average over the solid angle:

$$\kappa \approx \kappa_0 + \tfrac{1}{3}\kappa_z + \tfrac{2}{3}\kappa_{xy}. \qquad (C7)$$

[1] K. Klitzing, G. Dorda, and M. Pepper, Phys. Rev. Lett. **45**, 494 (1980).

[2] D. C. Tsui, H. L. Stormer, and A. C. Gossard, Phys. Rev. Lett. **48**, 1559 (1982).

[3] M. P. Lilly, K. B. Cooper, J. P. Eisenstein, L. N. Pfeiffer, and K. W. West, Phys. Rev. Lett. **83**, 824 (1999).

[4] R. Du, D. Tsui, H. Stormer, L. Pfeiffer, K. Baldwin, and K. West, Solid State Commun. **109**, 389 (1999).

[5] B. E. Feldman, M. T. Randeria, A. Gyenis, F. Wu, H. Ji, R. J. Cava, A. H. MacDonald, and A. Yazdani, Science **354**, 316 (2016).

[6] V. Celli and N. D. Mermin, Phys. Rev. **140**, A839 (1965).

[7] Y. Iye, L. E. McNeil, and G. Dresselhaus, Phys. Rev. B **30**, 7009 (1984).

[8] J. Alicea and L. Balents, Phys. Rev. B **79**, 241101 (2009).

[9] B. I. Halperin, Jpn. J. Appl. Phys. (1962–1981) **26**, 1913 (1987).

[10] Z. Tesanović and B. I. Halperin, Phys. Rev. B **36**, 4888 (1987).

[11] K. Behnia, L. Balicas, and Y. Kopelevich, Science **317**, 1729 (2007).

[12] L. Li, J. G. Checkelsky, Y. S. Hor, C. Uher, A. F. Hebard, R. J. Cava, and N. P. Ong, Science **321**, 547 (2008).

[13] H. B. Nielsen and M. Ninomiya, Phys. Lett. B **130**, 389 (1983).

[14] D. T. Son and B. Z. Spivak, Phys. Rev. B **88**, 104412 (2013).

[15] A. A. Burkov, Phys. Rev. Lett. **113**, 247203 (2014).

[16] S. A. Parameswaran, T. Grover, D. A. Abanin, D. A. Pesin, and A. Vishwanath, Phys. Rev. X **4**, 031035 (2014).

[17] J. Xiong, S. K. Kushwaha, T. Liang, J. W. Krizan, M. Hirschberger, W. Wang, R. J. Cava, and N. P. Ong, Science **350**, 413 (2015).

[18] H.-Z. Lu and S.-Q. Shen, Phys. Rev. B **92**, 035203 (2015).

[19] Z. Song, J. Zhao, Z. Fang, and X. Dai, Phys. Rev. B **94**, 214306 (2016).

[20] P. Rinkel, P. L. Lopes, and I. Garate, Phys. Rev. Lett. **119**, 107401 (2017).

[21] C.-L. Zhang, S.-Y. Xu, C. M. Wang, Z. Lin, Z. Z. Du, C. Guo, C.-C. Lee, H. Lu, Y. Feng, S.-M. Huang, G. Chang, C.-H. Hsu, H. Liu, H. Lin, L. Li, C. Zhang, J. Zhang, X.-C. Xie, T. Neupert, M. Z. Hasan, H.-Z. Lu, J. Wang, and S. Jia, Nat. Phys. **13**, 979 (2017).

[22] S. M. Young, S. Zaheer, J. C. Y. Teo, C. L. Kane, E. J. Mele, and A. M. Rappe, Phys. Rev. Lett. **108**, 140405 (2012).

[23] Z. Wang, Y. Sun, X.-Q. Chen, C. Franchini, G. Xu, H. Weng, X. Dai, and Z. Fang, Phys. Rev. B **85**, 195320 (2012).

[24] B.-J. Yang and N. Nagaosa, Nat. Commun. **5**, 4898 (2014).

[25] A. A. Burkov and L. Balents, Phys. Rev. Lett. **107**, 127205 (2011).

[26] X. Wan, A. M. Turner, A. Vishwanath, and S. Y. Savrasov, Phys. Rev. B **83**, 205101 (2011).

[27] H. Weng, C. Fang, Z. Fang, B. A. Bernevig, and X. Dai, Phys. Rev. X **5**, 011029 (2015).

[28] S.-M. Huang, S.-Y. Xu, I. Belopolski, C.-C. Lee, G. Chang, B. Wang, N. Alidoust, G. Bian, M. Neupane, C. Zhang, S. Jia, A. Bansil, H. Lin, and M. Z. Hasan, Nat. Commun. **6**, 7373 (2015).

[29] B. Q. Lv, N. Xu, H. M. Weng, J. Z. Ma, P. Richard, X. C. Huang, L. X. Zhao, G. F. Chen, C. E. Matt, F. Bisti, V. N. Strocov, J. Mesot, Z. Fang, X. Dai, T. Qian, M. Shi, and H. Ding, Nat. Phys. **11**, 724 (2015).

[30] S.-Y. Xu, I. Belopolski, N. Alidoust, M. Neupane, G. Bian, C. Zhang, R. Sankar, G. Chang, Z. Yuan, C.-C. Lee, S.-M. Huang, H. Zheng, J. Ma, D. S. Sanchez, B. Wang, A. Bansil, F. Chou, P. P. Shibayev, H. Lin, S. Jia, and M. Z. Hasan, Science **349**, 613 (2015).

[31] S. Nie, G. Xu, F. B. Prinz, and S. C. Zhang, Proc. Natl. Acad. Sci. USA **114**, 10596 (2017).

[32] V. A. Miransky and I. A. Shovkovy, Phys. Rep. **576**, 1 (2015).

[33] I. A. Shovkovy, in *Strongly Interacting Matter in Magnetic Fields* (Springer, Berlin, 2013), pp. 13–49.

[34] B. Roy and J. D. Sau, Phys. Rev. B **92**, 125141 (2015).

[35] X.-T. Zhang and R. Shindou, Phys. Rev. B **95**, 205108 (2017).

[36] A. A. Soluyanov, D. Gresch, Z. Wang, Q. Wu, M. Troyer, X. Dai, and B. A. Bernevig, Nature (London) **527**, 495 (2015).

[37] Y. Xu, F. Zhang, and C. Zhang, Phys. Rev. Lett. **115**, 265304 (2015).

[38] Z. Song, Y. Xu, S. Nie, H. Weng, Z. Fang, and X. Dai, arXiv:1512.05084.

[39] L. Hedin, Phys. Rev. **139**, A796 (1965).

[40] I. V. Lerner and Y. E. Lozovik, J. Low Temp. Phys. **38**, 333 (1980).

[41] P. A. Lee and T. M. Rice, Phys. Rev. B **19**, 3970 (1979).

[42] T. P. Devereaux and R. Hackl, Rev. Mod. Phys. **79**, 175 (2007).

[43] A. A. Abrikosov, Phys. Rev. B **58**, 2788 (1998).

[44] A. H. MacDonald, arXiv:cond-mat/9410047.

[45] K. E. Cahill and R. J. Glauber, Phys. Rev. **177**, 1857 (1969).